PHYSICAL REVIEW C VOLUME 26, NUMBER 5 NOVEMBER 1982

Proximity potential for heavy ion reactions on deformed nuclei

A. J. Baltz
Brookhaven National Laboratory, Upton, New York 11973

B. F. Bayman
University of Minnesota, Minneapolis, Minnesota 55455
and Brookhaven National Laboratory, Upton, New York 11973

(Received 13 July 1982)

The proximity potential is applied to the coupled-channels analysis of the inelastic scattering of heavy ions. It is shown that a suitably chosen proximity potential accurately reproduces the effect of a folding-model interaction between spherical nuclei. The heavy-ion Woods-Saxon potential is then considered as the result of a folding procedure and presented as an optional form for a proximity type potential. An analysis of the collision between spherical and deformed nuclei shows that, while the proximity potential well reproduces the folding model for this system, the proximity and center-line potentials lead to the extraction of significantly different values of high-multipole deformations. Formulas appropriate to the proximity interaction between two deformed nuclei are also presented.

[NUCLEAR REACTIONS $^{152}Sm(^{16}O,^{16}O')^{152}Sm$, calculated $\sigma(0^+,2^+,4^+,6^+)$ in coupled channels with deformed proximity potential; determined β_6.]

I. INTRODUCTION

The usual treatment of the deformed optical model for analysis of the inelastic scattering of heavy ions involves a potential which is a function of the distance between the nuclear surfaces along a line connecting the nuclear centers. Several authors,[1-3] using various approaches, have shown that this "center-line potential" is geometrically inadequate, especially if either or both of the nuclear surfaces have high-multipole deformations. Yet, despite its inadequacy, the center-line potential continues to be commonly used. This may be because the center-line potential works fairly well for the most commonly measured quadrupole deformation parameters, and none of the more sophisticated procedures are perceived as being either definitive (they still contain serious geometrical approximations) or easily related to the Woods-Saxon potential.

We have adapted the proximity potential[4,5] to give an improved treatment of the interaction between deformed nuclei. In this paper we work out a quantitatively adequate form of the deformed proximity potential, suitable for use with a coupled-channels reaction code in the analysis of inelastic scattering data above the Coulomb barrier. A major objective is to be able to extract reliably higher deformed multipole moments from such data. The deformed potential calculated in the folding model will serve as a geometrically exact benchmark to evaluate the accuracy of the proximity potential prescriptions.

We begin in Sec. II with a discussion of the spherical proximity potential and its relationship to the folding model. Analytical results are presented to illuminate the general form of the proximity potential and its relationship to the Woods-Saxon potential. Section III contains the development of the proximity potential for a spherical projectile on a deformed target and an evaluation of its validity. A set of inelastic scattering data is reanalyzed to demonstrate the importance of the present geometric treatment. In Sec. IV we consider the use of the proximity potential when both nuclei involved in the collision are deformed. Section V relates the present treatment to previous work and presents conclusions.

II. THE SPHERICAL PROXIMITY POTENTIAL AND THE FOLDING-MODEL POTENTIAL

The proximity potential as discussed by Blocki *et al.*[4] and by Brink and Stancu[5] is based on a

Thomas-Fermi treatment of the energy density of the ion-ion system. However we are interested in the tail of the potential for inelastic scattering analysis, and it is in just that region that the Thomas-Fermi method breaks down. Thus we will frame our development in terms of a model which should have its greatest validity in the tail of the potential, namely, the folding model. We are not particularly interested in the normalization of the basic ingredients of the folding model since the object of our consideration is the geometry of the deformed heavy-ion potential. The normalization can be obtained from a fit to data. In this section we assume that both the projectile and target are spherical. We take a single folding approach in which the nucleon-projectile optical potential (obtained empirically) is folded over the density of the target. We have for the folded potential V_F

$$V_F(R)=\int d^3r\, V_P(\vec{r}-\vec{R})\rho_T(\vec{r})\ , \tag{1}$$

where $V_P(\vec{r}-\vec{R})$ is the nucleon-projectile real optical potential and $\rho(\vec{r})$ is the target density (see Fig. 1). This integral may be evaluated exactly on a computer. To obtain its proximity form we follow the approach taken by Brink and Stancu in the related Thomas-Fermi problem. Owing to spherical symmetry Eq. (1) can be reduced to a two-dimensional integral over r_T and r_P (Fig. 2)

$$V(R)=\frac{2\pi}{R}\int r_T\,dr_T\,r_P\,dr_P\,V_P(r_P-R_P)\rho_T(r_T-R_T)\ , \tag{2}$$

with the limits of integration

$$r_T+r_P>R>|r_R-r_P|\ .$$

From this form Brink and Stancu obtain a two-term proximity potential

$$V_{P2}(R)=2\pi\frac{R_TR_P}{(R_T+R_P+S)}\times\left[\epsilon_0(S)+\frac{R_TR_P}{2R_TR_P}\epsilon_1(S)\right] \tag{3}$$

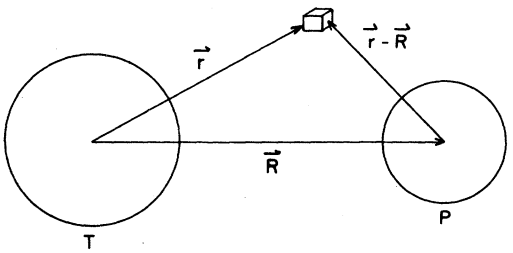

FIG. 1. Coordinates and volume element for the folding potential.

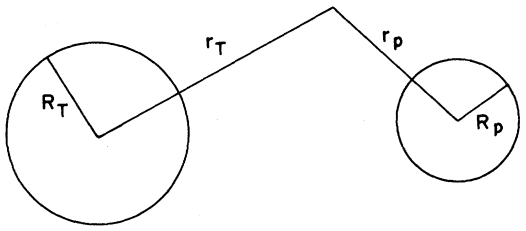

FIG. 2. Coordinates for a two-dimensional integral in the folding model.

with

$$\epsilon_n(S)=\int_S^\infty t^n e(t)dt \tag{4}$$

and, in our folding-potential case,

$$e(t)=\int_{-\infty}^{\infty}V_S(u)\rho(t-u)du\ . \tag{5}$$

In (3), S is the distance between the nuclear surfaces along the line between the centers. This form contains the next correction for finite curvature, in comparison to the more approximate form of Blocki *et al.*,

$$V_{P1}(R)=2\pi\frac{R_TR_P}{R_T+R_P}\epsilon_0(S)\ . \tag{6}$$

If we assume that both the nucleon-projectile potential and the target density have the same Fermi function form (with the same diffuseness a)

$$V_S(r_T)=\frac{V_P^0}{1+\exp[(r_T-R_T)/a]}\ , \tag{7}$$

$$\rho(r_p)=\frac{\rho_T{}^0}{1+\exp[(r_P-R_P)/a]}\ , \tag{8}$$

then the integral in (5) is equal to

$$e(t)=V_P^0\rho_T^0\frac{t}{\exp(t/a)-1}\ . \tag{9}$$

Brink[6] suggested this form for the one-term proximity version of the folding potential Eq. (6), which becomes

$$V_{P1}^F(R)=2\pi V_P^0\rho_T^0\frac{R_TR_P}{R_T+R_P}\times\int_{R-R_T-R_P}^{\infty}\frac{t\,dt}{\exp(t/A)-1}\ . \tag{10}$$

We have adapted Eq. (9) also for the two-term proximity potential, Eq. (3), and obtain

$$V_{P2}^{F}(R)=2\pi V_P^0\rho_T^0\frac{R_TR_P}{R}\left[\int_{R-R_T-R_P}^{\infty}\frac{t\,dt}{\exp(t/A)-1}+\frac{R_T+R_P}{2R_TR_P}\int_{R-R_T-R_P}^{\infty}\frac{t^2dt}{\exp(t/A)-1}\right]. \quad (11)$$

To test the validity of the proximity potential approximation we have made comparisons of the one- and two-term proximity potentials generated by Eqs. (10) and (11) with exact results obtained by numerical folding on a computer. Five representative cases are taken, spanning the region of heavy-ion reactions: $^{16}O+^{16}O$, $^{16}O+^{58}Ni$, $^{16}O+^{208}Pb$, $^{58}Ni+^{208}Pb$, and $^{208}Pb+^{208}Pb$. In all cases r_0 is set to 1.2 and a to 0.65 for both target and projectile Woods-Saxon densities.

The results seen in Fig. 3 are conclusive: The proximity potential in its two-term form is in excellent agreement with the folding model for all heavy-ion reactions, not only in shape, but in absolute magnitude. Furthermore, with a slightly increased normalization, the one-term proximity potential is also essentially identical to the folding model. Brink and Stancu[5] make the statement that the one-term proximity potential should be a less accurate approximation in the folding model than in their extended Thomas-Fermi case, but in fact our accuracy is comparable to their case. The two-term expression is even more suited to the folding model than to the more complicated angle dependent Thomas-Fermi case of Brink and Stancu.

While the folded potential is an attractive geometrical model for describing the real part of the heavy-ion optical potential, the fact is that for historical reasons the phenomenological potential most used in analyzing heavy-ion data has been the Woods-Saxon potential. It is amusing to do the inverse proximity potential problem, to obtain the form of the single nucleon density and single nucleon optical potential, which, when folded, would

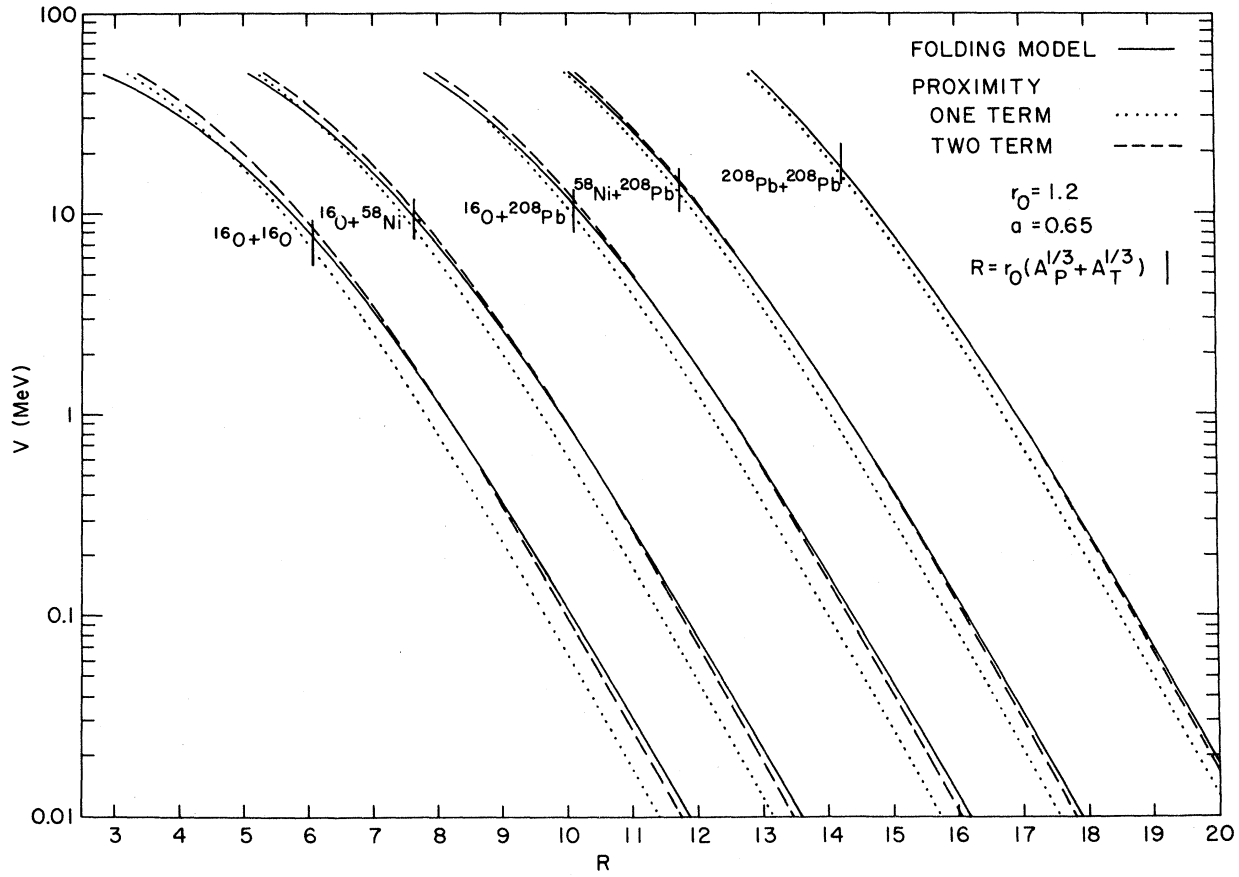

FIG. 3. Comparison of proximity and folding model calculations of the ion-ion potential. Both V_0 and ρ_0 are normalized to unity.

yield a Woods-Saxon potential in the proximity approximation. We will limit ourselves to the one-term proximity potential which is analytically tractable. Then we assume a proximity potential solution of the form

$$V_{P1}^{N}(R)=2\pi\frac{R_T R_P}{R_T+R_P}\epsilon_0^W(S)$$
$$=2\pi\frac{R_T R_P}{R_T+R_P}\frac{C}{\left[1+\exp\frac{R-R_T-R_P}{a}\right]}$$
$$=2\pi\frac{R_T R_P}{R_T+R_P}\int_{R-R_T-R_P}^{\infty}e(t)dt\ , \quad (12)$$

where $\epsilon_0^W(S)$ is a universal function of the ion-ion separation

$$S=R-R_T-R_P\ .$$

The function $e(t)$ that satisfies (12) may immediately be written down as the normalized first derivative of a Fermi (Woods-Saxon) function

$$e(t)=\frac{C}{a}\frac{\exp(t/a)}{(1+\exp(t/a))^2}\ . \quad (13)$$

Thus the universal slab on slab force is a surface force for the Woods-Saxon potential. To find the radial forms $f_v(r)$ and $f_\rho(r)$ for the density and potential which generate $e(t)$,

$$V^W(r)=V_0^W f_v(r)\ , \quad (14)$$

$$\rho^W(r)=\rho_0^W f_\rho(r)\ , \quad (15)$$

we rewrite Eq. (5) in the form

$$e(t)=\frac{C}{a}\frac{\exp(t/a)}{(1+\exp(t/a))^2}$$
$$=V_0^W\rho_0^W\int_{-\infty}^{\infty}f_v(u)f_\rho(t-u)du\ . \quad (16)$$

Obviously one solution of this integral equation is to take $f_\rho(r)$ as a surface peaked function of the same form as $e(t)$ and f_v as a δ function. This corresponds to a δ shell potential folded over a surface nucleon density. Of course the converse, a δ shell density folded over a surface nucleon potential, is also a solution. However a more interesting solution is one in which we require the same functional form

$$f_v(x)=f_\rho(x)=f(x)\ , \quad (17)$$

yielding the nonlinear integral equation

$$\int_{-\infty}^{\infty}f(u)f(t-u)du$$
$$=\frac{C}{aV_0^W\rho_0^W}\frac{\exp t/a}{(1+\exp(t/a))^2}\ . \quad (18)$$

We may solve for $f(x)$ using Fourier transforms and the convolution theorem (Appendix A), to obtain

$$f(x)=\frac{1}{a}\left[\frac{C}{V_0^W\rho_0^W}\right]^{1/2}\frac{1}{\pi^2}\left[\frac{2}{\pi}\right]^{1/4}$$
$$\times\int_0^{\infty}\sqrt{u}\,[\mathrm{csch}(u)]^{1/2}\cos\left[\frac{xu}{\pi a}\right]du\ . \quad (19)$$

If, for convenience, we let

$$C=\frac{a^2V_0^W\rho_0^W}{N^2}\ , \quad (20)$$

then

$$f(x)=\frac{1}{N\pi^2}\left[\frac{2}{\pi}\right]^{1/4}$$
$$\times\int_0^{\infty}\sqrt{u}\,[\mathrm{csch}(u)]^{1/2}\cos\left[\frac{xu}{\pi a}\right]du\ , \quad (21)$$

$$e(t)=\frac{V_0^W\rho_0^W a}{N^2}\frac{\exp(t/a)}{(1+\exp(t/a))^2}$$
$$=V_0^W\rho_0^W\int_{-\infty}^{\infty}f(u)f(t-u)du\ ,$$

and

$$V_{P1}^W(R)=2\pi\frac{R_T R_P}{R_T+R_P}\frac{V_0^W\rho_0^W}{N^2}a^2\frac{1}{(1+\exp(S/a))}\ . \quad (22)$$

The physical implication of these results is of interest in interpreting the successful use of the Woods-Saxon parametrization in fitting heavy-ion data. What generates a Woods-Saxon potential in the one-term proximity approximation is the folding of a surface nucleon density with a surface nucleon potential, both of which have the radial form of Eq. (21). This universal surface function is evaluated numerically and plotted in Fig. 4 as a function of x/a. Also plotted in Fig. 4 are approximate derivative Fermi function representations of the surface term $a'=1/1.4$ and $a'=a/1.33$ where a is the diffusivity of the Woods-Saxon potential generated from the folding of these surface forms. Thus a Woods-Saxon potential of diffusivity a implies effective surface densities of $\sim 0.7a$ in the two ions. This makes it hard to understand the use of

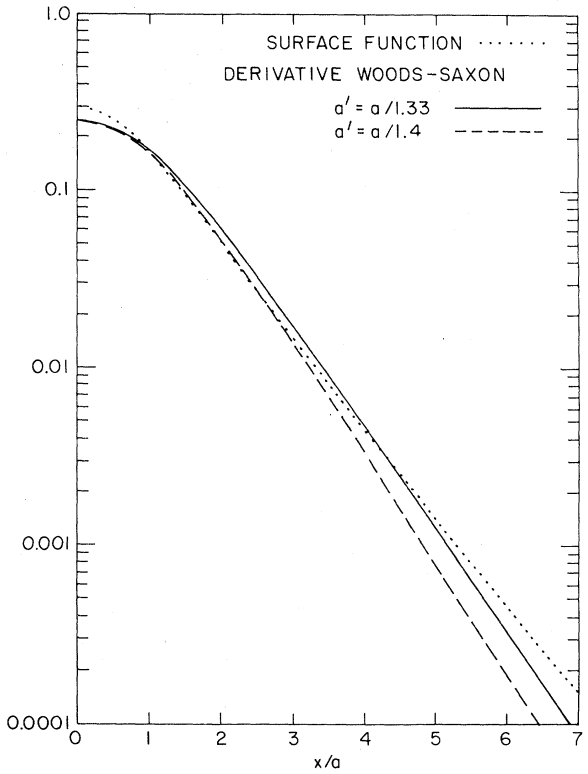

FIG. 4. Comparison of an arbitrarily normalized surface function $f(s/a)$, Eq. (24), with derivative Woods-Saxon functions of s/a'.

real potential diffusivities of ~ 0.5 in analysis of heavy-ion data when the diffusivity of finite nuclei is ~ 0.6.

III. PROXIMITY POTENTIAL FOR THE INTERACTION BETWEEN A DEFORMED AND A SPHERICAL NUCLEUS

Suppose we have a spherical projectile of radius R_P, and an axially symmetric target whose shape is given by

$$R_T(\theta)=r_0[1+\sum_L \beta_L Y_L^0(\cos\theta)] \, . \tag{23}$$

The center-line prescription takes the interaction between these two nuclei to be of the form

$$V(R,\theta)=V_0 f(R-R_P-R_T(\theta)) \, , \tag{24}$$

where f is a radial form factor, often taken to be a Woods-Saxon shape

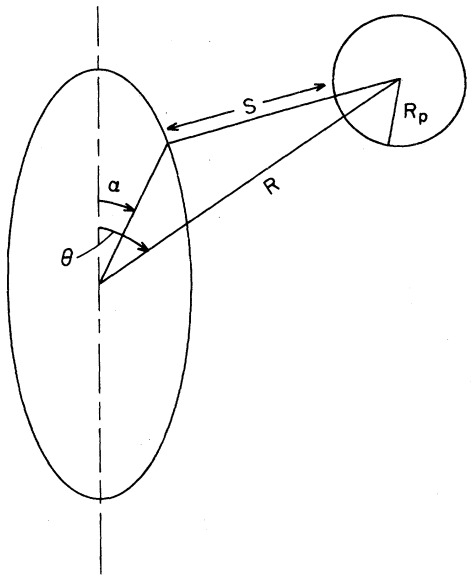

FIG. 5. Geometry needed for the proximity interaction between spherical and deformed nuclei.

$$f(R-R_P-R_T(\theta))=\left[1+\exp\frac{R-R_P-R_T(\theta)}{a}\right]^{-1} .$$

The geometry associated with the use of the proximity interaction between these nuclei is shown in Fig. 5. The interaction is a function of the distance S between the surfaces along the shortest line connecting them, and of the radii of curvature at the opposite ends of this line. For given values of R and θ, the angle α in Fig. 5 is obtained by solving the equation

$$\frac{\cos(\theta-\alpha)}{R_T(\alpha)}+\frac{\sin(\theta-\alpha)}{R_T'(\alpha)}=\frac{1}{R} \, , \tag{25}$$

where

$$R_T'(\alpha)\equiv(dR_T/d\alpha) \, .$$

Equation (25) expresses the condition that the line of minimum length S is perpendicular to both surfaces. In general, (25) must be solved numerically. Once α has been determined, we get S from

$$S=[R^2+R_T^2(\alpha)-2RR_T\cos(\theta-\alpha)]^{1/2}-R_P \, . \tag{26}$$

The principal radii of curvature of the target surface at a point whose polar angle is α are given by

$$R_1(\alpha)=\left|\frac{[R_T^2(\alpha)+[R_T'(\alpha)]^2]^{3/2}}{R_T^2(\alpha)+2[R_T'(\alpha)]^2-R_T(\alpha)R_T''(\alpha)}\right|, \tag{27a}$$

$$R_2(\alpha)=\left|\frac{R_T(\alpha)\sin\alpha[R_T^2(\alpha)+[R_T'(\alpha)]^2]^{1/2}}{R_T'(\alpha)\cos\alpha-R_T(\alpha)\sin\alpha}\right| \tag{27b}$$

(see Appendix B for derivations). The principal radii of curvature of the gap between the nuclei are then

$$\frac{R_1(\alpha)R_p}{R_1(\alpha)+R_p}$$

and

$$\frac{R_2(\alpha)R_p}{R_2(\alpha)+R_p},$$

respectively, so the one-term proximity interaction between the nuclei shown in Fig. 5 is

$$V_{P1}(R,\theta)=2\pi\left[\frac{R_1(\alpha)R_P}{R_1(\alpha)+R_P}\right]^{1/2}\left[\frac{R_2(\alpha)R_P}{R_2(\alpha)+R_P}\right]^{1/2}\epsilon_0(S) \tag{28}$$

[cf. Eq. (9)].

To find a two-term generalization of (28), we compare the two-term and one-term forms of the spherical proximity potential [Eqs. (6) and (9)]. This suggests that a reasonable form for a deformed $V_{p2}(R,\theta)$ would be

$$V_{P2}(R,\theta)=2\pi\left[\frac{R_1(\alpha)R_P}{R_1(\alpha)+R_P+S}\right]^{1/2}\left[\frac{R_2(\alpha)R_P}{R_2(\alpha)+R_P+S}\right]^{1/2}$$
$$\times\left[\left[\epsilon_0(S)+\frac{R_1(\alpha)+R_P}{2R_1(\alpha)R_P}\epsilon_1(S)\right]\left[\epsilon_0(S)+\frac{R_2(\alpha)+R_P}{2R_2(\alpha)R_P}\epsilon_1(S)\right]\right]^{1/2}. \tag{29}$$

In (28) and (29), $\epsilon_0(S)$ and $\epsilon_1(S)$ are the one-dimensional slab-on-slab functions given by (4), (5), and (9).

Up to now we have only really treated the real part of the optical potential. One does not expect the folding picture to have much validity for the imaginary potential. We will assume, however, that the geometrical picture of the deformed proximity potential can be taken over to the imaginary potential in conjunction with a Woods-Saxon or other empirical potential for the slab-on-slab radial form. As we saw in Sec. II, the Woods-Saxon potential form can be seen to arise out of a surface-surface folding. This picture does not seem geometrically unreasonable for the generation of a heavy-ion imaginary potential. Adopting a one-term proximity potential treatment of the deformed imaginary potential we obtain

$$W_{P1}(R,\theta)=W(S)\left[\frac{R_1(\alpha)R_P}{R_1(\alpha)+R_P}\frac{R_2(\alpha)R_P}{R_2(\alpha)+R_P}\right]^{1/2}\frac{R_T+R_P}{R_PR_T}$$
$$=W(S)\left[\frac{R_1(\alpha)R_2(\alpha)}{(R_1(\alpha)+R_P)(R_2(\alpha)+R_P)}\right]^{1/2}\frac{(R_T+R_P)}{R_T}, \tag{30}$$

where $W(S)$ is any empirical potential form and R_T is the spherical radius of the deformed radius $R_1(\alpha)$.

This potential form might also be utilized for the real potential if one did not want to abandon empirical Woods-Saxon potentials, but nevertheless wanted to provide a geometrically more correct treatment of deformation.

As we did in Sec. II we would like to use the folding model as a benchmark to help us understand the proximity potential. We will evaluate the angle dependent folding potential by folding a spherical Woods-Saxon projectile density over a deformed Woods-Saxon target density with a δ function interaction

$$V(R,\theta)=\int \frac{d^3r}{\left[1+\exp\left[\frac{|\vec{R}-\vec{r}|-R_p}{a}\right]\right]\left[1+\exp\left[\frac{r-R_T(\alpha)}{a}\right]\right]} . \quad (31)$$

Coordinates are shown in Fig. 6. The small effect of the a dependent density falling off radially rather than perpendicularly to the surface will be ignored in the folding calculations.

For comparison we will calculate the angular momentum components of the angle dependent optical potentials for both folded and proximity potentials

$$V_l(R)=2\pi \int_{\theta=0}^{\pi} \sin\theta \, d\theta \, Y_0^l(\theta,0)V(R,\theta) . \quad (32)$$

These components are evaluated on a computer using 8 Gauss points per quadrant.

To investigate various aspects of the deformed proximity potential we have chosen a case for which data exist and for which a coupled-channels analysis[7] has been performed: 72 MeV $^{16}O+^{152}Sm$. Geometrically, this is a typical case, a light heavy-ion projectile on a more massive deformed target.

Figure 7 shows a comparison of optical components generated by the folding model and by the one-term and two-term proximity potentials. The two-term proximity potential is practically indistinguishable from the folding model both in radial shape of all the components and in absolute magnitude. The one-term proximity potential is slightly lower in magnitude for all components.

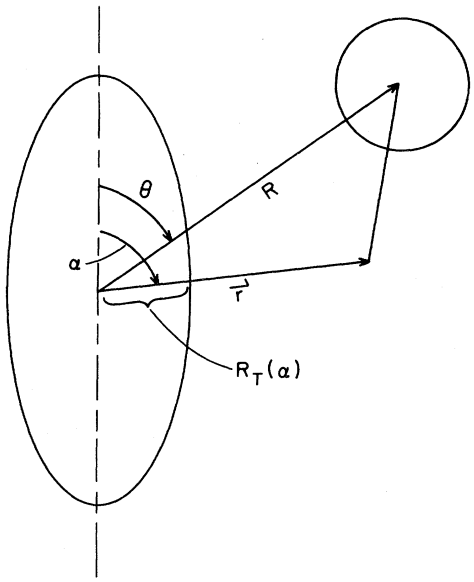

FIG. 6. Coordinate system for folding spherical and deformed nuclei using a zero-range potential.

Since the V_0 component is ultimately fit to elastic data, the ratio of computed components to the $l=0$ component must be reliably calculated for reliable extraction of multipole moments. Figure 8 shows these ratios indicating that the one-term proximity potential is as good or better than the two-term proximity when renormalized. We will thus only use the one-term proximity potential in the following calculations.

The crucial point of this whole development is how the proximity model treatment differs from the center-line prescription when higher multipole components are extracted. We have plotted in Fig. 9 the ratios of angular momentum components to the real monopole potential using the center-line prescription and the Woods-Saxon proximity potential of Eq. (19). Assuming the Woods-Saxon proximity potential has the more correct relative geometry for the given deformation lengths ($\beta_2 R_N{}^2=1.65$, $\beta_4 R_N{}^4=0.29$), we find that V_4/V_0 and V_6/V_0 are significantly overpredicted in the center-line prescription for the $\beta_4 R_N{}^4$ value of 0.29, implying a true value somewhat larger. In fact there is a discrepancy between this value obtained in Kim's heavy-ion analysis and the values of $\beta_4 R^4=0.52$ and 0.53 from electron scattering and Coulomb excitation, respectively. If we keep $\beta_2 R_N{}^2$ at 1.65 and set $\beta_4 R^4$ to 0.52 then we obtain the ratios seen in Fig. 10 for the Woods-Saxon proximity model which are very close to the ratios of the center-line prescription in Fig. 9 probed by Kim's analysis.

To test these observations further, coupled-channels calculations have been performed for this case using the coupled-channels code QUICC.[8] In Fig. 11 the solid line is a repetition of Kim's original calculation, using the center-line prescription and $\beta_2 R_N{}^2=1.65$, $\beta_4 R_N{}^4=0.29$, which fits the data. The dotted line is a Woods-Saxon proximity potential calculation with the same parameters except that the real and imaginary potential strengths are reduced by 6% to fit the elastic scattering. The dashed line is a Woods-Saxon proximity potential

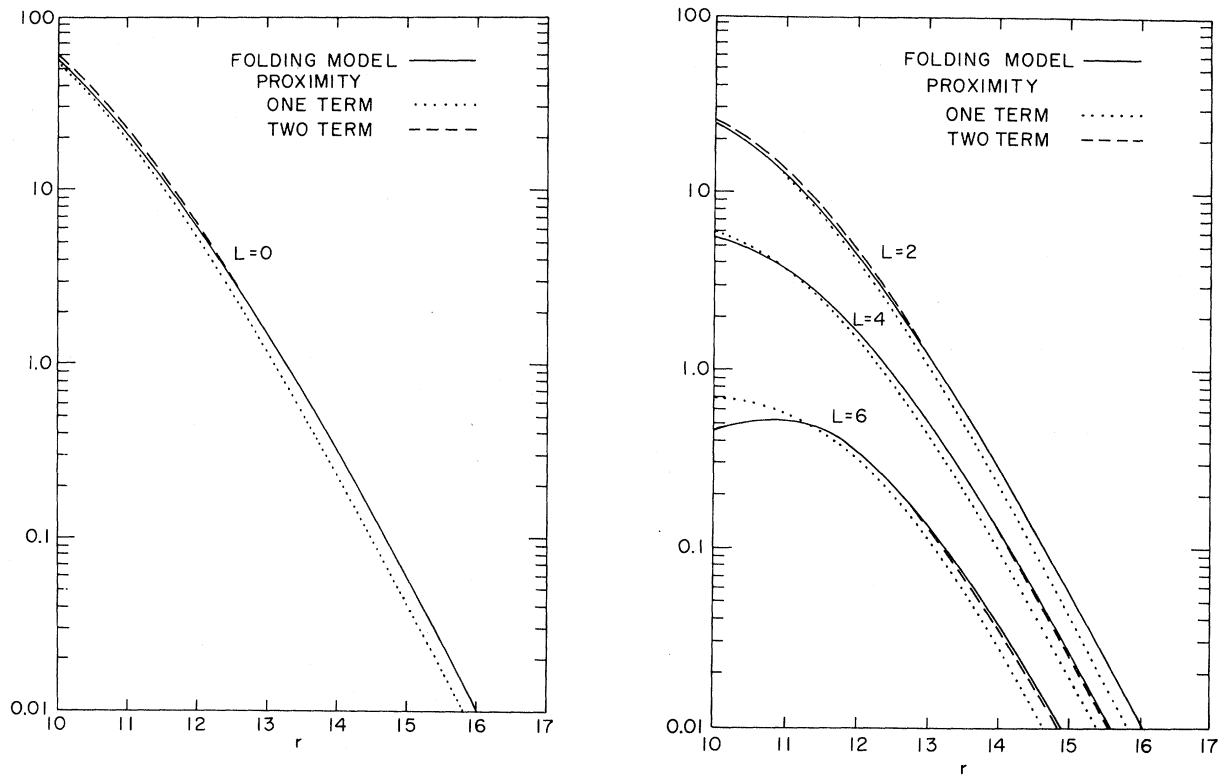

FIG. 7. Comparison of optical model components generated in the folding model and in the one- and two-term proximity models. V_0 and ρ_0 have been set to unity, while the r_0 and a for the densities are the same as the optical model parameters of Ref. 7.

calculation with $\beta_4 R_N{}^4=0.52$ and all other parameters the same as the previous. Clearly the proximity potential calculation with $\beta_4 R_N{}^4=0.52$ corresponds better to the center-line calculation of $\beta_4 R_N{}^4=0.29$ and thus to the data. Using the more correct proximity prescription has caused the discrepancy with the electron scattering and Coulomb excitation results to disappear.

IV. PROXIMITY POTENTIAL FOR THE INTERACTION BETWEEN TWO AXIALLY SYMMETRIC DEFORMED NUCLEI

We consider only the orientation degrees of freedom of the colliding nuclei. Let $\hat{n}_1$ and $\hat{n}_2$ be unit vectors along the symmetry axes of the two nuclei, with polar coordinates $\theta_1\phi_1$ and $\theta_2\phi_2$. The relative vector $\vec{R}$, from the mass center of nucleus 1 to the mass center of nucleus 2, has polar coordinates $\theta\phi R$. The total wave function can be written in the form

$$\Psi(\theta_1\phi_1;\theta_2\phi_2;\theta\phi R)=\sum_{\substack{J,S\\ I_1,I_2\\ l}} U_{I_1I_2SlJ}(R)\{[Y^{I_1}(\theta_1\phi_1)Y^{I_2}(\theta_2\phi_2)]^S Y^l(\theta\phi)\}^J_0 . \tag{33}$$

A single term in (33) corresponds to a state in which the nuclei have angular momenta I_1 and I_2, channel spin S, relative orbital angular momentum l, and the system has total angular momentum J. The Schrödinger equation can be expressed as a set of coupled ordinary differential equations for the radial functions $U_{I_1I_2SlJ}(R)$. The coupling matrix elements in this set of equations are

$$M(R)=\langle\{[Y^{I_1}(\theta_1\phi_1)Y^{I_2}(\theta_2\phi_2)]^S Y^l(\theta\phi)\}^J_0 | V(\theta_1\phi_1;\theta_2\phi_2;\theta\phi R) | \{[Y^{I_1'}(\theta_1\phi_1)Y^{I_2'}(\theta_2\phi_2)]^{S'} Y^{l'}(\theta\phi)\}^J_0\rangle . \tag{34}$$

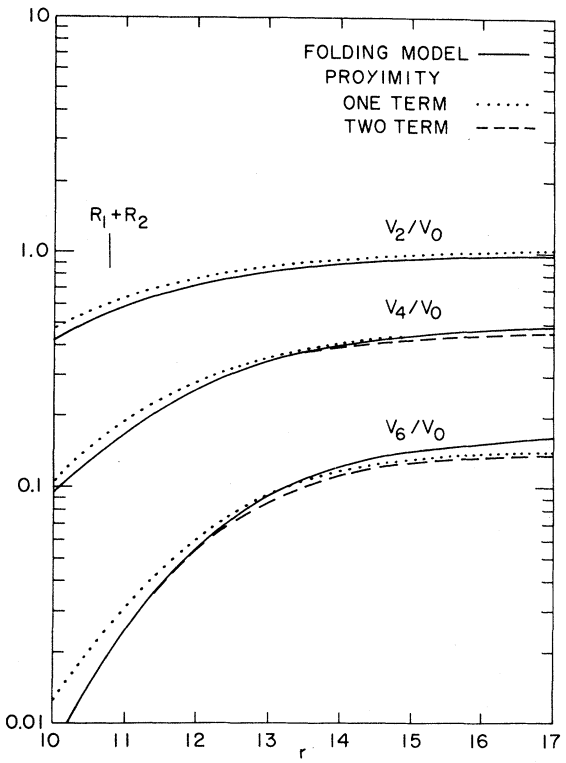

FIG. 8. Ratios of $L=2,4,6$ components to the $L=0$ component of the various calculations in Fig. 7.

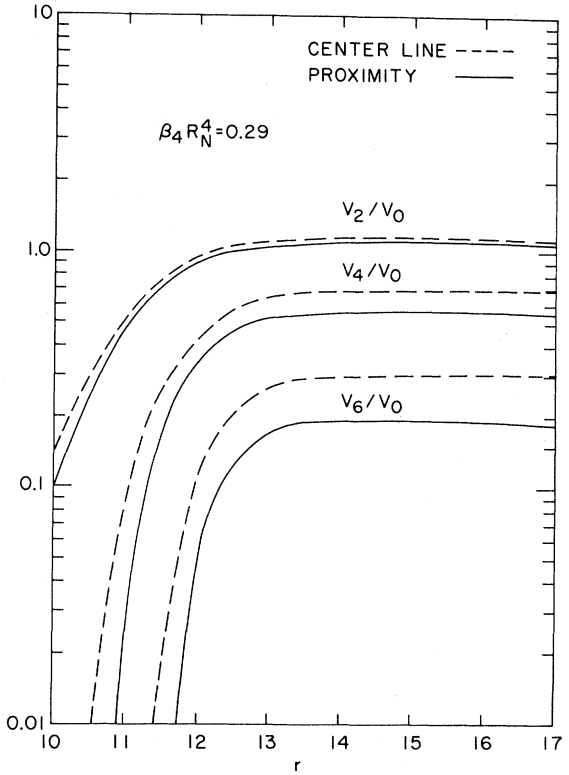

FIG. 9. Comparison of ratios of $L=2,4,6$ components of the Woods-Saxon potential of Ref. 7 to the $L=0$ component using the center-line prescription and the one-term proximity prescription.

Here V is the interaction between the nuclei and the integrations are over $\theta_1,\phi_1,\theta_2,\phi_2,\theta,\phi$ for fixed R.

$M(R)$ in (34) depends upon nine quantum numbers $I_1,I_2,S,l,I_1',I_2',S',l'$, and J. Straightforward angular momentum recoupling allows us to express it in terms of simpler functions $m_{L_1L_2L}(R)$:

$$M(R)=\sum_{L_1L_2L} i^{l+l'-L+I_1+I_1'-L_1+I_2+I_2'-L_2}\left[\frac{(2l+1)(2l'+1)(2I_1+1)(2I_1'+1)(2I_2+1)(2I_2'+1)}{(4\pi)^3(2L+1)(2L_1+1)(2L_2+1)}\right]^{1/2}$$

$$\times[(Sl)_J(S'l')_J\,|\,(SS')_L(ll')_L]_0[(I_1I_2)_S(I_1'I_2')_{S'}\,|\,(I_1I_1')_{L_1}(I_2I_2')_{L_2}]_L$$

$$\times(ll'00\,|\,L\,0)(I_1I_1'00\,|\,L_1 0)(I_2I_2'00\,|\,L_2 0)m_{L_1L_2L}(R)\,, \tag{35a}$$

$$m_{L_1L_2L}(R)\equiv\int \sin\theta\,d\theta\,d\phi\,\sin\theta_1 d\theta_1 d\phi_1\,\sin\theta_2 d\theta_2 d\phi_2 V(\theta_1\phi_1;\theta_2\phi_2;\theta\phi R)$$

$$\times\{[Y^{L_1}(\theta_1,\phi_1)Y^{L_2}(\theta_2\phi_2)]^L Y^L(\theta\phi)\}_0^0\,. \tag{35b}$$

Here L_1, L_2, and L play the roles of "angular momentum transfers" to nuclei 1, 2, and the relative motion, respectively. We expect V in (35b) to be unchanged if the directions of $\hat{n}_1$, $\hat{n}_2$, and $\hat{R}$ are all reversed, and this has the consequence that $m_{L_1L_2L}(R)$ vanishes unless L_1+L_2-L is even. If V is unchanged when $\hat{n}_1$ is replaced by $-\hat{n}_1$, then (35b) vanishes unless L_1 is even, and similarly for $\hat{n}_2$ and L_2.

We can use the rotational invariance of V to reduce the six-dimensional integral of (35b) to a three-dimensional integral. Every configuration $(\hat{n}_1,\hat{n}_2,\hat{R})$ can be obtained by applying a rigid-body rotation to a "reference" configuration $(\hat{n}_1',\hat{n}_2',\hat{Z})$ in which $\hat{R}$ points along the $\hat{z}$ axis and $\hat{n}_1'$ lies in the x-z plane with

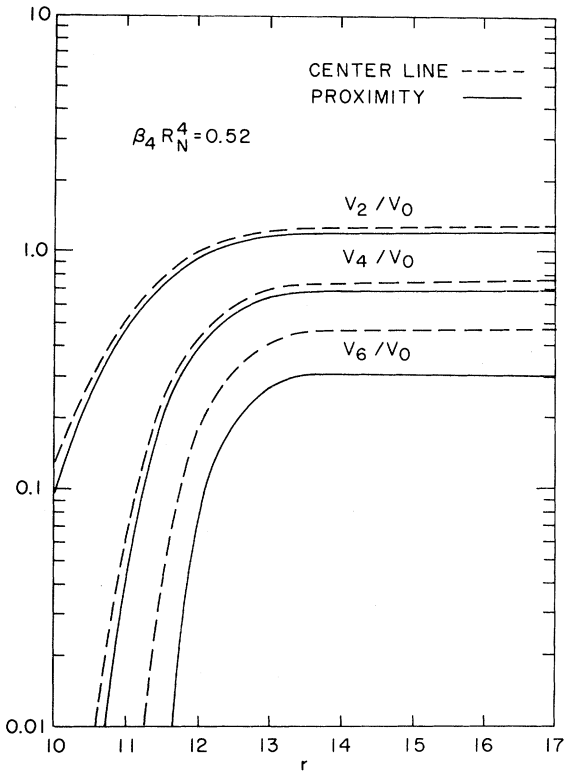

FIG. 10. As in Fig. 9 with $\beta_4 R^4 = 0.52$.

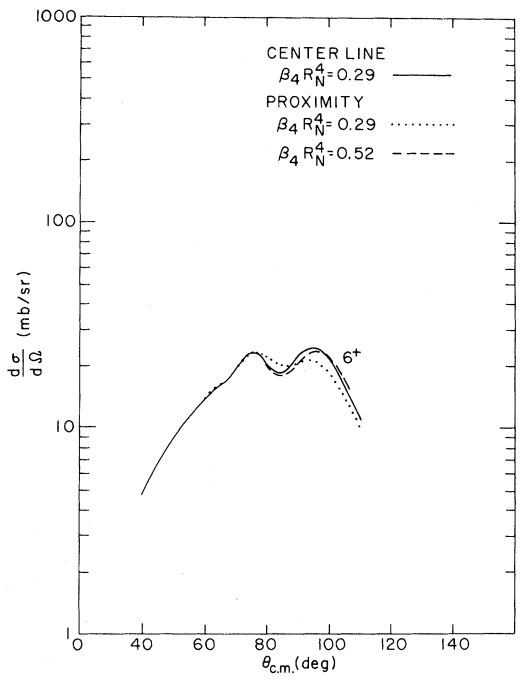

FIG. 11. Comparison of ^{152}Sm(^{16}O,^{16}O′)^{152}Sm(6^+) angular distributions. See text.

$(\hat{n}_1')_x \geq 0$ (see Fig. 12). The polar coordinates in this reference configuration are $(\theta_1',0;\theta_2'\phi_2';00R)$. Let $(\alpha\beta\gamma)$ be the Euler angles of the rotation from $(\hat{n}_1',\hat{n}_2',\hat{z})$ to $(\hat{n}_1,\hat{n}_2,\hat{R})$. Then we can use the six angles $(\alpha,\beta,\gamma,\theta_1',\theta_2',\phi_2')$ as our six integration variables instead of $(\theta_1\phi_1;\theta_2\phi_2;\theta\phi)$. The advantage of this choice is that the spherically symmetric integrand of (35b) is independent of $(\alpha\beta\gamma)$, so that the $(\alpha\beta\gamma)$ integration can be done immediately and simply yields a factor of $8\pi^2$:

$$m_{L_1L_2}(R)=8\pi^2\int \sin\theta_1' d\theta_1' \sin\theta_2' d\theta_2' d\phi_2' V(\theta_1'0;\theta_2'\phi_2';00R)\{[Y^{L_1}(\theta_1',0)Y^{L_2}(\theta_2'\phi_2')]^L Y^L(0,0)\}_0^0$$

$$=(-i)^L\frac{8\pi^2}{\sqrt{4\pi}}\int \sin\theta_1' d\theta_1' \sin\theta_2' d\theta_2' d\phi_2' V(\theta_1'0;\theta_2'\phi_2';00R)[Y^{L_1}(\theta_1'0)Y^{L_2}(\theta_2'\phi_2')]_0^L$$

$$=i^{L_1+L_2-L}[\pi(2L_1+1)(2L_2+1)]^{1/2}\sum_m (L_1L_2m\,-m\,|\,L0)\int_0^\pi \sin\theta_1' d\theta_1' \sin\theta_2' d\theta_2' d^{L_1}_{m,0}(\theta_1') d^{L_2}_{-m,0}(\theta_2')$$

$$\times\int_{-\pi}^{\pi} d\phi_2' e^{-im\theta_2'} V(\theta_1'0;\theta_2'\phi_2'00R)\,. \tag{35c}$$

The reduced rotation matrices used in (35c) are defined by

$$d^L_{m,0}(\theta)=\sum_n (-1)^n \frac{L![(L-m)!(L+m)!]^{1/2}}{n!(L+m-n)!(L-n)!(n-m)!}\left[\cos\frac{\theta}{2}\right]^{2L+m-2n}\left[\sin\frac{\theta}{2}\right]^{2n-m}$$

$$=(-1)^m d^L_{-m,0}(\theta) \tag{36a}$$

and are related to the spherical harmonics by

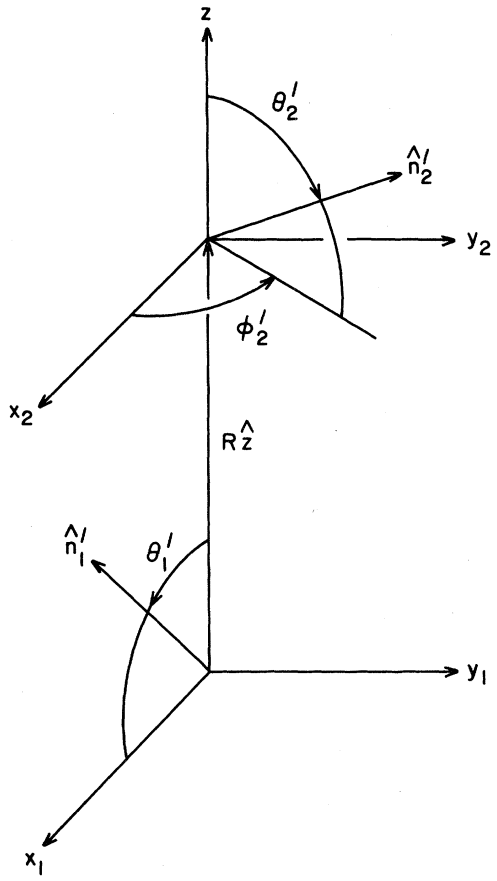

FIG. 12. The nuclei in a "reference configuration." $\vec{R}$ lies along the z axis and $\hat{n}_1'$ is in the x-z plane with $(\hat{n}_1')_x \geq 0$.

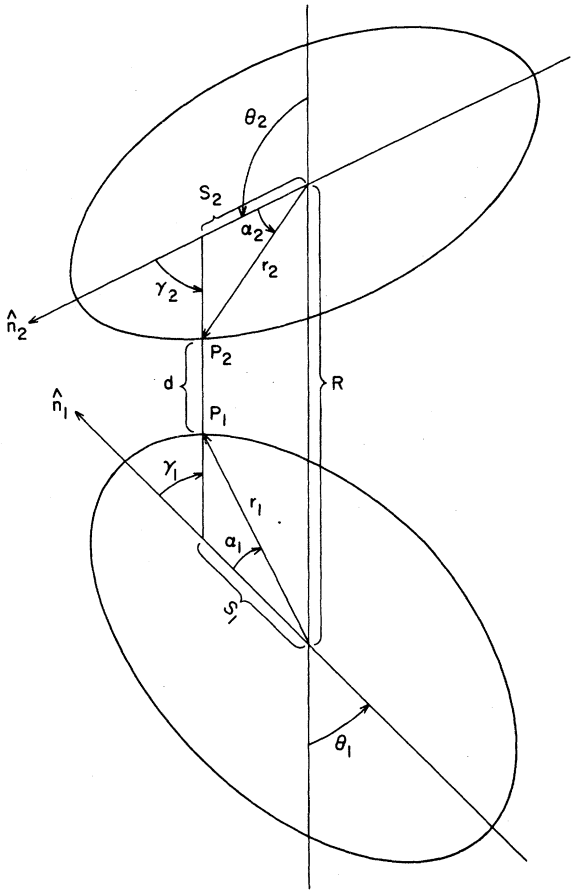

FIG. 13. The two nuclei, shown in the special case in which $\phi_2=0$. P_1 and P_2 are at opposite ends of the shortest line connecting the two surfaces.

$$Y_m^L(\theta,\phi)=i^L\left[\frac{2l+1}{4\pi}\right]^{1/2} d_{m,0}^L(\theta)e^{im\phi} . \tag{36b}$$

Because the nuclei are axially symmetric, V is an even function of ϕ_2'. The fact that L_1+L_2-L is even then allows us to rewrite (35c) as

$$m_{L_1L_2}(R)=i^{L_1+L_2-L}[16\pi(2L_1+1)(2L_2+1)]^{1/2}\sum_{m\geq 0}(-1)^m\frac{(L_1L_2m\,-m\mid L\,0)}{1+\delta m,0}$$
$$\times\int_0^\pi \sin\theta_1 d\theta_1 \sin\theta_2 d\theta_2 d_{m,0}^{L_1}(\theta_1)d_{m,0}^{L_2}(\theta_2)$$
$$\times\int_0^\pi d\phi_2 \cos m\phi_2\, V(\theta,0;\theta_2\phi_2;00R) . \tag{37}$$

Note that we have dropped the primes on the integration variables in (37).

To evaluate the proximity potential V in the integrand of (37), we must be able to determine the points P_1 and P_2 on the surfaces of the two nuclei at opposite ends of the shortest line connecting the surfaces. Figure 13 shows the geometry of the problem, in the special case in which $\phi_2=0$. Note that the line connecting P_1 and P_2 is perpendicular to both surfaces and, because of the axial symmetry, passes through both axes $\hat{n}_1$ and $\hat{n}_2$. P_1 and P_2 must be found by an iterative process. We have found that the following scheme converges rapidly:

(1) Choose a value for α_1 and calculate s_1 and γ_1 using the formulas

$$s_1=\frac{r_1 r_1'}{r_1' \cos\alpha_1 - r_1 \sin\alpha_1} \quad \left[r_1' = \frac{dr_1}{d\alpha_1} \right] , \tag{38a}$$

$$\gamma_1 = \arctan\left[\frac{r_1 \sin\alpha_1}{r_1 \cos\alpha_1 - s_1} \right] . \tag{38b}$$

This determines a cone whose axis is $\hat{n}_1$ and whose generators all pierce surface 1 at a right angle.

(2) Find the generator that intersects $\hat{n}_2$, the axis of surface 2. Its azimuthal angle, in the body-fixed coordinate system of nucleus 1, is given by

$$\delta_1 = \arctan\left[\frac{vw \pm u(u^2+v^2-w^2)^{1/2}}{uw \mp v(u^2+v^2-w^2)^{1/2}} \right] ,$$

where

$$u \equiv (s_1 - R\cos\theta_1)\sin\theta_2 \sin\phi_2 ,$$

$$v \equiv [R\sin\theta_2 \cos\phi_2 + s_1(\sin\theta_1 \cos\theta_2 - \cos\theta_1 \sin\theta_2 \cos\phi_2)] ,$$

$$w \equiv R \sin\theta_1 \sin\theta_2 \sin\phi_2 \cot\gamma_1 .$$

The distance between the axes along this generator is

$$t = \frac{s_1 \sin\theta_1 \sin\phi_2}{\sin\gamma_1(\sin\delta_1 \cos\phi_2 - \cos\theta_1 \cos\delta_1 \sin\phi_2) - \cos\gamma_1 \sin\theta_1 \sin\phi_2}$$

and the intersection with $\hat{n}_2$ occurs at a distance

$$s_2 = \frac{\sin\gamma_1 \sin\delta_1}{\sin\theta_2 \sin\phi_2} t \tag{39a}$$

from the center of nucleus 2, at an angle γ_2 given by

$$\gamma_2 = \arccos((\cos\theta_1 \sin\gamma_1 \cos\delta_1 + \sin\theta_1 \cos\gamma_1)\sin\theta_2 \cos\phi_2 + \sin\gamma_1 \sin\delta_1 \sin\theta_2 \sin\phi_2$$
$$+ (-\sin\theta_1 \sin\gamma_1 \cos\delta_1 + \cos\theta_1 \cos\gamma_1)\cos\theta_2) . \tag{39b}$$

(3) If the original choice for α_1 was correct, then s_2 and γ_2 calculated in (39) would be related parametrically to an angle α_2 by a set of equations corresponding to (37), since the generator constructed perpendicular to surface 1 would also be perpendicular to surface 2. If the s_2 and γ_2 given by (39) are not related in this way, a new choice of α_1 is made and steps 1 and 2 are repeated. After two passes through this procedure, interpolation can be used to guide further choices of α_1.

Once we have determined α_1 and α_2 (equivalently P_1 and P_2 of Fig. 13), we can calculate the four-principal radii of curvature at these points (Ref. 27)

$$R_{i1} = \left| \frac{[r_i^2 + (r_i')^2]^{3/2}}{r_i'' r_i - 2(r_i')^2 - r_i^2} \right| , \tag{40a}$$

$(i = 1,2)$

$$R_{i2} = \left| \frac{r_i \sin\alpha_i [r_i^2 + (r_i')^2]^{1/2}}{r_i' \cos\alpha_i - r_i \sin\alpha_i} \right| . \tag{40b}$$

Then the product of the principal radii of curvatures of the gap between the surfaces is given by

$$\bar{R}_1 \bar{R}_2 = \frac{R_{11} R_{12} R_{21} R_{22}}{(R_{11}+R_{21})(R_{12}+R_{22}) + \sin^2\psi (R_{11}-R_{12})(R_{21}-R_{22})} . \tag{41a}$$

Here ψ is the angle between the planes defined by the line P_1P_2 and the two symmetry axes $\hat{n}_1,\hat{n}_2$. It is given by

$$\psi=\arccos\left[\frac{\cos\theta_1\cos\theta_2+\sin\theta_1\sin\theta_2\cos\phi+\cos\gamma_1\cos\gamma_2}{\sin\gamma_1\sin\gamma_2}\right] . \tag{41b}$$

Finally, the distance between P_1 and P_2 is

$$d=t-r_1\frac{\sin\alpha_1}{\sin\gamma_1}-r_2\frac{\sin\alpha_2}{\sin\gamma_2} .$$

This determines all the information needed to evaluate the proximity potential V for the configuration $(\theta_1 0;\theta_2\phi_2;00R)$. We can then perform the integration (37) and use (35a) to calculate the coupling matrix element $M(R)$.

V. RELATION TO PREVIOUS WORK AND CONCLUSIONS

We have mentioned three previous improved treatments of the interaction of a spherical projectile on a deformed target. The approach of Moffa *et al.*[1] was a full folding of a spherical density with a deformed density, but the deformation of the density was only taken to first order as was appropriate for the vibrational nuclei which they considered. Hendrie's work[2] considered the nuclei as touching, for his correction to the multipole moments generated by an angular shift relative to the center-line prescription. However he did not include effects of the angular change in the force due to the changing radius of curvature. Randrup and Vaagen[3] showed the importance of the local radius of curvature as well as the effective angular shift, but considered the effect for only the β_2 deformation and for only one separation of the two nuclei. Furthermore, their approximations for the radii of curvature, while qualitatively instructive, are not quantitatively useful for extracting multipole moments. For example, at $\theta=0$, these author's first-order approximation for the local radius of curvature $R_1(\theta=0)$ yields $0.6216R$ for their parameters while our exact value is $0.8050R$ for the same parameters.

In conclusion we feel that we have presented a quantitatively adequate treatment of the deformed optical potential for extraction of multipole moments from heavy-ion induced inelastic scattering on deformed nuclei.

APPENDIX A

We define the following normalization for the Fourier cosine transformations:

$$G(\alpha)=\left[\frac{2}{\pi}\right]^{1/2}\int_0^\infty g(u)\cos(\alpha u)du , \tag{A1}$$

$$g(X)=\left[\frac{2}{\pi}\right]^{1/2}\int_0^\infty G(\alpha)\cos(\alpha X)d\alpha . \tag{A2}$$

We wish to solve

$$\frac{C}{aV_0^W\rho_0^W}\frac{\exp(x/a)}{[1+\exp(x/a)]^2}=\frac{C}{4aV_0^W\rho_0^W}\operatorname{sech}^2\left[\frac{x}{2a}\right] =\int_{-\infty}^\infty f(u)f(x-u)du . \tag{A3}$$

If we define the convolution of g with itself as

$$g*g=\frac{1}{\sqrt{2\pi}}\int_0^\infty g(u)g(x-u)du , \tag{A4}$$

then the following convolution theorem holds for the Fourier transforms

$$T\{g*g\}=(T\{g\})^2 . \tag{A5}$$

If we write Eq. (A3)

$$\frac{1}{\sqrt{2\pi}}\frac{C}{4aV_0^W\rho_0^W}\operatorname{sech}^2\left[\frac{x}{2a}\right] =\frac{1}{\sqrt{2\pi}}\int_{-\infty}^\infty f(u)f(x-u)du , \tag{A6}$$

then we have

$$(T\{f\})^2=T\left[\frac{1}{\sqrt{2\pi}}\frac{C}{4aV_0^W\rho_0^W}\operatorname{sech}^2\left[\frac{x}{2a}\right]\right]$$
$$=\frac{2}{\pi}\int_0^\infty\frac{1}{\sqrt{2\pi}}\frac{C}{4aV_0^W\rho_0^W}\times\operatorname{sech}^2\left[\frac{x}{2a}\right]\cos(yx)dx$$
$$=\frac{1}{\sqrt{2\pi^3}}\frac{C}{V_0^W\rho_0^W}\int_0^\infty\operatorname{sech}^2\left[\frac{x}{2a}\right]\times\cos\left[2ay\frac{x}{2a}\right]\frac{dx}{2a}\,, \tag{A7}$$

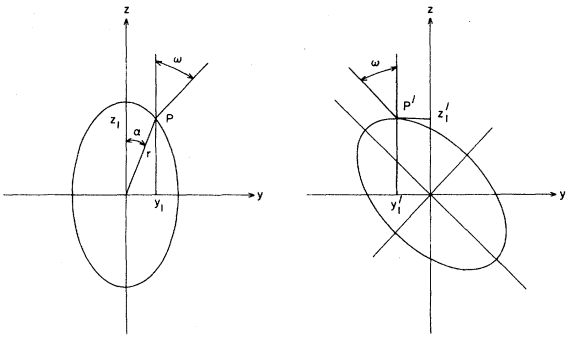

FIG. 14. (a) A surface of revolution whose symmetry axis is the z axis. A line is drawn normal to the surface at P. (b) The surface has been rotated about the x axis until the normal line is vertical.

$$(T\{f\})^2=\frac{1}{\sqrt{2\pi^3}}\frac{C}{V_0^W\rho_0^W}\pi ay\operatorname{csch}(\pi ay)\,, \tag{A8}$$

$$T\{f\}=\left[\frac{1}{2\pi^3}\right]^{1/4}\left[\frac{C}{V_0^W\rho_0^W}\right]^{1/2}\sqrt{\pi ay}\,(\operatorname{csch}(\pi ay))^{1/2}\,, \tag{A9}$$

and (A2) implies

$$f(x)=\left[\frac{2}{\pi}\right]^{1/2}\left[\frac{1}{2\pi^3}\right]^{1/4}\left[\frac{C}{V_0^W\rho_0^W}\right]^{1/2}\int_0^\infty\sqrt{\pi ya}\,(\operatorname{csch}(\pi ay))^{1/2}\cos(xy)dy\,, \tag{A10}$$

$$f(x)=\frac{1}{a\pi^2}\left[\frac{2}{\pi}\right]^{1/4}\left[\frac{C}{V_0^W\rho_0^W}\right]^{1/2}\int_0^\infty\sqrt{u}\,(\operatorname{csch}(u))^{1/2}\cos\left[\frac{xu}{\pi a}\right]du\,. \tag{A11}$$

APPENDIX B

Figure 14(a) shows a surface of revolution whose shape is specified by

$$z=f[(x^2+y^2)^{1/2}]$$
$$=f(y)\text{ in the }x=0\text{ plane}\,. \tag{B1}$$

Point P has Cartesian coordinates $(0,y_1,z_1)$. The angle ω between the z axis and the normal to the surface at P is given by

$$\omega=\arctan(-f'(y_1))\,. \tag{B2}$$

Now rotate the surface counterclockwise about the x axis through angle ω. This will carry P into a new point P' [see Fig. 14(b)] whose coordinates are

$$\cos\omega+y_1\sin\omega=\frac{z_1-y_1f'(y_1)}{\{1+[f'(y_1)]^2\}^{1/2}}\,,$$
$$y_1\cos\omega-z_1\sin\omega=\frac{y_1+z_1f'(y_1)}{\{1+[f'(y_1)]^2\}^{1/2}}\,. \tag{B3}$$

A plane tangent to the surface at P' is horizontal. The equation of the rotated surface is

$$z\cos\omega-y\sin\omega$$
$$=f\{[x^2+(y\cos\omega+z\sin\omega)^2]^{1/2}\}\,. \tag{B4}$$

It is now straightforward to calculate the partial derivatives of z with respect to x and y at P':

$$\left.\frac{\partial z}{\partial x}\right|_{P'}=\left.\frac{\partial z}{\partial y}\right|_{P'}=0\,,$$
$$\left.\frac{\partial^2 z}{\partial x^2}\right|_{P'}=\frac{f'(y_1)}{y_1\{1+[f'(y_1)]^2\}^{1/2}}\,,$$
$$\left.\frac{\partial^2 z}{\partial y^2}\right|_{P'}=\frac{f''(y_1)}{(1+[f'(y_1)]^2)^{3/2}}\,,$$

from which we calculate the two principal radii of curvature at P' to be

$$R_1=\left|\frac{1}{\left[\frac{\partial^2 z}{\partial y^2}\right]_{P'}}\right|=\left|\frac{\{1+[f'(y_1)]^2\}^{3/2}}{f''(y_1)}\right|,$$

$$R_2=\left|\frac{1}{\left[\frac{\partial^2 z}{\partial x^2}\right]_{P'}}\right|=\left|\frac{y_1\{1+[f'(y_1)]^2\}^{1/2}}{f'(y_1)}\right|. \quad \text{(B5)}$$

If we express the shape of the surface in Fig. 14(a) in polar coordinates, we find that

$$f'(y_1)=\frac{r'\cos\alpha - r\sin\alpha}{r'\sin\alpha + r\cos\alpha},$$

$$f''(y_1)=\frac{r''r-2(r')^2-r^2}{[r'\sin\alpha + r\cos\alpha]^3}.$$

If these expressions are substituted into (B5), we get $R_1(\alpha)$ and $R_2(\alpha)$ of (27).

[1]P. J. Moffa, C. B. Dover, and J. P. Vary, Phys. Rev. C 16, 1857 (1977).
[2]D. L. Hendrie, Phys. Rev. Lett. 31, 478 (1973).
[3]J. Randrup and J. S. Vaagen, Phys. Lett. 77B, 170 (1978).
[4]J. Blocki, J. Randrup, W. J. Swiatecki, and C. F. Tsang, Ann. Phys. (N.Y.) 105, 427 (1977).
[5]D. M. Brink and Fl. Stancu, Nucl. Phys. A299, 321 (1978).
[6]D. M. Brink, J. Phys. C 37, 5 (1976).
[7]B.-T. Kim, Phys. Lett. 80, 353 (1979).
[8]A. J. Baltz, Phys. Rev. C 25, 240 (1982).